Coupled Land-Sea Warming Dominates the Net Land Carbon Uptake Variability in the Greater Bay Area of South China

Bingxiong Fan[1,2] and Yangfan Li[1,2] [iD]

[1]State Key Laboratory of Marine Environmental Science, College of the Environment and Ecology, Xiamen University, Xiamen, China, [2]Southern Marine Science and Engineering Guangdong Laboratory (Zhuhai), Zhuhai, China

Abstract As Earth's warming is driven by anthropogenic activities (e.g., urbanization), land and ocean warming significantly affect the net carbon uptake (NCU) of global ecosystems. However, the driving mechanism of coupled land-sea warming on the NCU under rapid urbanization in coastal areas remains poorly understood. Here, we used long-term remote sensing and meteorological observation data combined with spatial analysis and multivariate statistical methods to study the impact of coupled land-sea warming and urbanization on land net primary productivity (LNPP, a proxy of the net land carbon uptake) in the Guangdong-Hong Kong-Macao Greater Bay Area (GBA), a rapidly urbanizing and climatically vulnerable area of South China. We found that the total LNPP decreased by 0.40 TgC from 1985 to 2015 and declined suddenly after 2003, driven by the reduced relative humidity and increased vapor pressure deficit (VPD). The increased VPD was caused by coupled land-sea warming, and the indirect effect ($\gamma = -0.51$, $p < 0.001$) of coupled land-sea warming on LNPP variability was much stronger than the direct effect ($\gamma = -0.16$, $p < 0.05$). In addition to the severe decline in the LNPP (0.20 TgC) induced by coupled land-sea warming, urbanization caused a large loss in LNPP (0.16 TgC), which accounted for 40% of the total LNPP loss. Our findings can support future predictions of regional carbon uptake and inform future climate change mitigation strategies to implement carbon peak and neutrality goals.

Plain Language Summary Climate warming driven by rapid industrialization and urbanization has altered the processes and functions of global ecosystems. However, how the interaction of land/sea warming affects vegetation productivity and the carbon cycle in coastal areas is not clear. Here, a cascading effect of coupled land-sea warming on the net carbon uptake (NCU) variability was detected in the Guangdong-Hong Kong-Macao Greater Bay Area (GBA), the area with the most rapid urbanization and climate warming in South China. Climate warming and urban sprawl, driven by urbanization, caused a consistent reduction in the net carbon uptake from 1985 to 2015 across all types of land cover in the GBA. A turning point of a sudden decline in net carbon uptake was detected when the vapor pressure deficit increased and the land/sea surface temperature sharply increased after 2003. An increased vapor pressure deficit, associated with coupled land-sea warming, was the primary driver of reduced net carbon uptake. Our findings can support future predictions of regional carbon sinks and inform future climate change mitigation strategies from a coupled land-sea warming perspective.

1. Introduction

Since the industrial revolution, large amounts of carbon dioxide have been released into the atmosphere through human activities, resulting in dramatic warming of the Earth in recent decades, further leading to frequent extreme events (e.g., heat waves, extreme precipitation, and extreme drought). In the process of global climate change, the land and ocean surface has warmed substantially owing to global warming (Frölicher et al., 2018; Sutton et al., 2007), which can affect land-sea carbon and water cycles, solar energy flow, and biological community composition, thereby, directly and indirectly influencing vegetation growth and productivity (Carnicer et al., 2019; Piao et al., 2008). Therefore, it is critical to understand how land and sea warming affects the ecosystem NCU (Ballantyne et al., 2012).

The challenge with exploring the effects of climate warming on the ecosystem NCU is that the driving mechanisms of climate warming are complex (e.g., warming and altered precipitation regimes, warming and land-sea evaporation change). They may be interactive or additive and often significantly modify vegetation productivity (Wu et al., 2021). Plant growth has significantly increased with the impact of climate warming in many areas of

Writing – original draft: Bingxiong Fan
Writing – review & editing: Bingxiong Fan, Yangfan Li

the globe, and the photosynthetic capacity and duration of the growing season have been significantly enhanced, resulting in increased carbon uptake in terrestrial ecosystems (Lucht et al., 2002). However, the effects of warming on plant carbon uptake may transition to negative effects once temperatures exceed a suitable ecophysiological threshold. A growing body of research suggests that reduced water supplies due to continued climate warming and decreased precipitation have limited plant growth and productivity (Humphrey et al., 2021; Ukkola et al., 2016; Wu et al., 2021; Zhao & Running, 2010).

Recently, increased vapor pressure deficit (VPD) has been considered an increasingly important driver of plant growth and productivity on the global scale, mainly caused by land warming (Bastos et al., 2013; Grossiord et al., 2020; Liu et al., 2017; Yuan et al., 2019). VPD describes the difference between the vapor pressure at saturation and the actual vapor pressure for a given temperature, determined by atmospheric relative humidity and temperature. An increase in VPD would likely constrain vegetation carbon uptake and water use in terrestrial ecosystems (Grossiord et al., 2020; Novick et al., 2016). However, there are different opinions on the drivers of VPD increase, some studies suggested that reduced soil moisture due to climate warming limit the land evapotranspiration, reduces the relative humidity, and thus raises the VPD (Humphrey et al., 2021; Massmann et al., 2019). Others indicated the increased VPD is caused by the increased temperature and reduced relative humidity owing to ocean warming (Byrne & O'Gorman, 2018). Most of the moisture over land is transported from the oceans, accounting for 35% of precipitation and 55% of evapotranspiration over land (Yuan et al., 2019), which determines VPD variation over land.

Coastal areas are the most intense land-sea interaction zones with complex climatic conditions. As the ocean becomes warmer, the land surface temperature is amplified (Byrne & O'Gorman, 2013; Sutton et al., 2007), and the relative humidity declines (Byrne & O'Gorman, 2018; Zappa et al., 2020), which results in an increase in VPD and affects human and land ecosystem health. Additionally, coastal ocean warming is closely linked to remarkable changes in coastal urban thermal environments, showing consistent trends of increases in land temperature and demonstrating the strong coupling of coastal oceans and lands under the influence of global warming and regional interactions of the coastal ocean, land, and the atmosphere (Hu et al., 2021). Therefore, coupled land-sea warming in coastal areas is becoming a significant topic for coastal research on global climate change. The coupled land-sea warming is defined as strong interactions between land and sea warming, which may be additive effects, antagonistic effects, or synergistic effects, that have a positive/negative impact on land net carbon uptake by altering atmospheric moisture and thermal conditions together. However, studies rarely focus on the effects of coupled land-sea warming on net ecosystem carbon uptake, and it remains unclear whether the coupled land-sea warming is the dominant driver of the interannual variability in land NUC in coastal areas.

Land NCU is also affected by the land use change (Wang et al., 2014). A new evaluation showed the urbanization-induced decrease in net primary production (NPP) offset 30% of the climate-driven increase at a global scale (Liu et al., 2019). As one of the important components of urbanization, urban land expansion and its effects on terrestrial NPP have been widely examined at a regional scale (Imhoff et al., 2004; Pei et al., 2013). Coastal areas with highly intensive urbanization are affected by the interaction of climate drivers and land use change. Here, our goals are to investigate (a) how the coupled land-sea warming affects carbon uptake variability in the GBA; and (b) how rapid urbanization can result in large NUC losses in coastal areas with highest intensive human activities. Therefore, it is necessary to explain which factor attributes more to coastal carbon uptake variability between climate-driven and urbanization-driven scenarios, which is critical in coastal areas to implement carbon neutrality.

2. Materials and Methods

2.1. Study Area

Our study area covers approximately 179,800 km^2 on the south coast of China, consists of Guangdong, Hong Kong, and Macau, and borders the Northern South China Sea (NSCS) (Figure 1). The prevailing climate in this region is subtropical, with an annual rainfall of 1,700 mm and an average annual temperature of 19 °C. The study area mostly belongs to the monsoon climate region, with rainfall and heat energy occurring in the same seasons, providing a favorable plant growth environment. The primary ecosystem types include evergreen broadleaf forest, evergreen needle leaf forest, mixed forest, and alpine shrub. Since the economic reform in 1978, the GBA region has witnessed rapid and unprecedented urbanization. In 2020, this region became one of the largest metropolitan
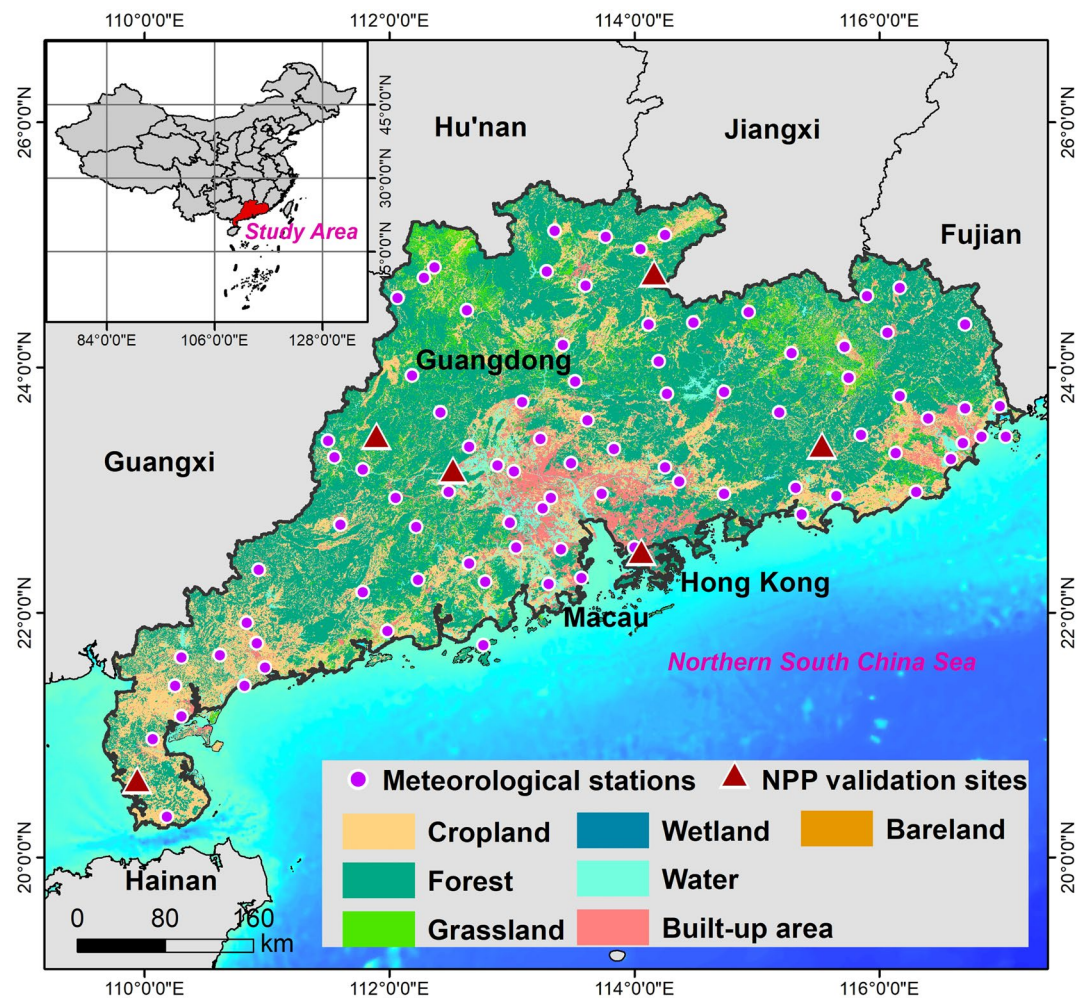
Figure 1. Location of meteorological stations, net primary productivity (NPP) validation sites, and land cover types in the study area.

areas in China, with urban areas five times larger than those in 2000. During 1982–2018, most of the regions in the NSCS warmed, and the sea surface temperature anomaly trend increased and was abnormally cold before 2000 but abnormally hot after 2000 (Figure S1 in Supporting Information S1). Such ocean warming phenomena were reported to be harmful to marine and terrestrial ecosystems and their associated biological systems (Arias-Ortiz et al., 2018; Smale et al., 2019; Tkachenko & Soong, 2017).

2.2. Data Sources

2.2.1. Multivariate NPP Data Sets and Accuracy Testing

We collected three NPP products from the global land surface satellite (GLASS) (http://www.glass.umd.edu/Download.html), multiresolution satellite remote sensing (MUSES) global vegetation productivity data set (https://zenodo.org/record/3996814#.YVSjOjFBw2w) and moderate-resolution imaging spectroradiometer (MODIS). The GLASS NPP product had a high temporal resolution (8 days over 1982–2018) and a spatial resolution of 0.05° and was derived by the eddy covariance—light use efficiency (EC-LUE) model with GLASS leaf area index (LAI)/photosynthetically active radiation (PAR) products, moisture stress, and air temperature, which were validated to be more continuous and complete in terms of their temporal and spatial distributions and have better accuracy than the MODIS NPP products (Yuan et al., 2007). To validate the accuracy of the GLASS NPP product in the GBA of South China, the carbon flux data set of observed sites (Din Hushan, Hong Kong, Zu Rong, Hei Shiding, Nan Wang, and Liu Jiashan, shown in Figure 1) was collected from the ChinaFLUX website

(http://www.chinaflux.org/) and Luo (1996). ChinaFLUX is a Chinese network of meteorological tower sites used to measure the exchanges of carbon dioxide, water vapor, and energy between the biosphere and atmosphere and has been widely used in ecosystem model validation (Hu et al., 2008; Yu et al., 2006). The validation results suggested that the GLASS NPP had better accuracy than the MUSES NPP in the GBA of South China (Figure S2 in Supporting Information S1); the squared R was 0.67 ($p < 0.01$), and the root mean square error (RMSE) was 20.93 gC/m^2/month.

2.2.2. Land Use/Cover Data Sets

The land use/cover maps of the Chinese land use/cover data set (CLUD) in 1985, 1990, 1995, 2000, 2005, 2010, and 2015 were obtained from the Resource and Environment Science and Data Center (http://resdc.cn/Default.aspx). The CLUD was extracted by visual interpretation after a series of preprocessing methods based on a variety of multispectral satellite data, which were validated with a 94.3% average classification accuracy in the six primary land cover categories (i.e., cropland, forest, grassland, water bodies, built-up areas, and wetland). We extracted the boundaries of built-up areas for 1985 and 2015 to analyze the urbanization-driven NPP losses near the NSCS.

The GlobeLand30 data set for 2000, 2010, and 2015 was obtained from the National Geomatics Center of China (http://www.globallandcover.com) to validate the accuracy of CLUD. The data set was produced using more than 20,000 Landsat and Chinese HJ-1 satellite images with resolutions of 30 m (Chen et al., 2017). Specifically, the MCD12Q1 data set from the IGBP classification scheme was obtained for 2000–2015 to analyze annual NPP variation in different land use/cover types because it had a more continuous time series than the CLUD. The annual NPP variation in different land use/cover types from 1985 to 2000 was based on the CLUD in 1985, 1990, and 1995. Considering the different spatial resolutions in NPP data and land use/cover data, we used the GALSS NPP data as a benchmark to resample the land use data with a higher resolution to 0.05° of spatial resolution.

2.2.3. Meteorological Data

The sea surface temperature (SST) and SST anomaly maps of the Coral Reef Temperature Anomaly Database (CoRTAD) from 1985 to 2015 were obtained from the National Oceanic and Atmospheric Administration's National Centers for Environmental Information (NOAA NCEI; https://www.ncei.noaa.gov/access/metadata/landing-page/bin/iso?id=gov.noaa.nodc:NCEI-CoRTADv6#Coverage), with a weekly temporal resolution and a spatial resolution of 4 km. We extracted the SST and SST anomaly data in the NSCS region to analyze the variability in the NSCS SST and reveal the phenomenon of ocean warming in the NSCS. The annual time series of atmospheric CO_2 concentration data at the South China Sea observatory was obtained from the NOAA Earth System Research Laboratory (NOAA ESRL; http://www.esrl.noaa.gov/gmd/ccgg/trends). Meteorological data over land were extracted from the HadISDH data set provided by the Met Office Hadley Center (https://www.metoffice.gov.uk/hadobs/hadisdh/) and the Chinese Resource and Environment Science and Data Center (https://www.resdc.cn/Default.aspx), and monthly temperature, specific humidity, and relative humidity were used to calculate the vapor pressure deficit over land (Harris et al., 2014).

2.3. Theil-Sen Median Trend Analysis and Turning Point Detection in the LNPP

Spatiotemporal trends in the LNPP from 1985 to 2015 in the Guangdong-Hong Kong-Macao region were analyzed at the pixel level using a robust nonparametric Theil-Sen median trend analysis method, which is widely applied to trend analyses of long-time series with nonnormal data, with the Mann-Kendall (M-K) method to check the significance of the data trends (Ding et al., 2020; Rajah et al., 2014). The functions are as follows:

$$Z = \begin{cases} \dfrac{S-1}{\sqrt{Var(S)}}, & if\ S > 0 \\ 0, & if\ S = 0 \\ \dfrac{S+1}{\sqrt{Var(S)}}, & if\ S < 0 \end{cases} \tag{1}$$

where Z is the standard normal test statistic, S is the M-K score, and $Var(S)$ is the variance of S. The M-K test statistic Z is approximately normally distributed when the sample size $n > 8$. If $Z > 0$, it signifies that there is

an increasing trend and vice versa. In our study, the threshold of Z scores used for testing significance over time was 1.96 at the 5% significance level ($\alpha = 0.05$), which provided both the significance and direction of the trend.

$$S = \sum_{i=1}^{n-1} \sum_{j=i+1}^{n} sig\,(x_j - x_i) \qquad (2)$$

$$Var(S) = \frac{n(n-1)(2n+5) - \sum_{i=1}^{m} t_i\,(t_i - 1)\,(2t_i + 5)}{18} \qquad (3)$$

where n is the number of data points; x_i and x_j are the data values in time series i and j ($j > i$), respectively; t_i is the number of ties of extent i; and $sig(x_j - x_i)$ is the sine function expressed as:

$$sig\,(x_j - x_i) = \begin{cases} 1, \; if \; x_j - x_i > 0 \\ 0, \; if \; x_j - x_i = 0 \\ -1, \; if \; x_j - x_i < 0 \end{cases} \qquad (4)$$

The Theil-Sen median slope estimator for estimating the slope of the trend in a sample with N pairs of data can be calculated as follows:

$$\beta_i = Median\left(\frac{x_j - x_k}{j - k}\right) \; and \; i = 1, \ldots, N, \qquad (5)$$

where x_j and x_k are the data values at times j and k ($j > k$), respectively.

We further used the BFAST01 toolbox (checking for one major break in the time series) in R software to detect whether there was a spatiotemporal turning point of annual LNPP during 1985–2015. The types of turning points include negative reversal, interrupted increase, positive reversal, and interrupted decrease (Bernardino et al., 2020). A negative reversal suggests a shift in the annual LNPP from an increasing trend to a decreasing trend around the turning point. An interrupted increase presents a shift in the annual LNPP from an increasing trend toward a faster or slower increase around the turning point. A positive reversal suggests a shift in the annual LNPP from a decreasing trend to an increasing trend around the turning point. An interrupted decrease presents a shift in the annual LNPP from a decreasing trend toward a faster or slower decrease around the turning point.

2.4. Isolating Impacts of Urbanization, Land Cover Change, and Climate Warming

Terrestrial ecosystems near the NSCS might be affected by multiple factors (primarily human activities, land cover change, and climate warming). Thus, the isolation of multiple factors was important to understand the influence of different factors on land carbon uptake. First, we divided the study area into three parts: urbanization dominance, land cover change (LCC) dominance, and climate dominance to minimize interference between the three drivers (Figure 2a). For urbanization-dominant areas, we extracted and overlaid the boundary of built-up areas in 1985 and 2015, and the area between the two boundaries was identified as urbanization-dominant (Figure 2b). For LCC-dominant areas, the area that has undergone a significant land cover change (except for conversion to the built-up area) was identified as LCC-dominant, for example, conversion between forest and grassland (Figure 2c). For climate-dominant areas, permanent natural land, which did not undergo land use change and was far away from human activities from 1985 to 2015, was identified as climate-dominant (Figure 2d).

2.5. Detecting the Effects of Coupled Land-Sea Warming on LNPP Variability

Temperature, precipitation, humidity, CO_2 concentration, VPD, and soil moisture are major drivers on the variation of vegetation productivity and carbon uptake, which has been indicated by numerous studies (Bastos & Fleischer, 2021; Liu et al., 2019; Runyon & Waring, 1994; Yang et al., 2008; Zhu et al., 2016). Land-sea environmental coupling could be considered as an important mechanism of net carbon uptake variability in the land-sea interface, especially when land surface temperature and dryness are amplified by ocean warming. Therefore, for our study area, a humid coastal area, we hypothesized that the land and neighboring ocean warming gradually
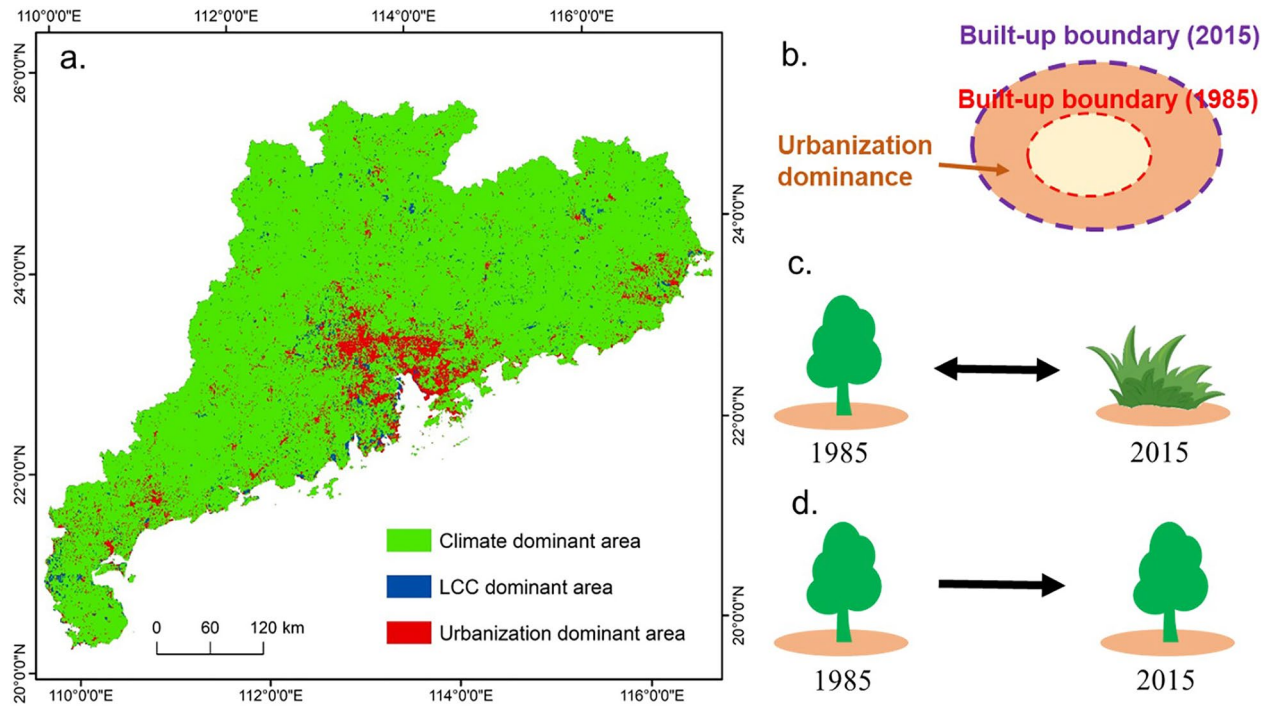
Figure 2. (a) Distribution of climate-dominant area, land cover change (LCC)-dominant area and urbanization-dominant area, (b)–(d) isolation methods of urbanization dominance, LCC dominance, and climate dominance.

became a major negative driver affecting LNPP. Then, focusing on climate-dominant areas, six environmental and climatic factors (mean annual sea surface temperature (SST), mean annual land surface temperature (LST), mean annual precipitation, atmospheric specific humidity (ASH), soil moisture content (SMC), and mean annual VPD) and two ecological factors (leaf area index and net primary production) were selected to build an empirical model and verify our hypothesis. A structural equation model (SEM) was adopted to test and quantify the interaction of climate factors, the effects of land and ocean warming on LNPP variability, and the relative importance of direct and indirect pathways among different drivers.

2.5.1. Anomaly Calculation and Sensitivity Analysis

Before SEM analysis, the anomalies of all factors from 1985 to 2015 were first calculated to analyze the effects of land-sea temperature change on LNPP variability and to make dimensionless factors comparable. The formula is as follows:

$$A_{ij} = \frac{X_{ij} - M_i}{SD_i} \tag{6}$$

where A_{ij} is the anomaly of factor i in year j, X_{ij} is the observed value of factor i in year j, M_i is the average value of factor i during 1985–2015, and SD_i is the standard deviation of factor i during 1985–2015. Then, the sensitivity analysis of the LNPP variation to drivers was applied to provide support for the SEM analysis. The sensitivity of the LNPP anomaly to a variable is defined as:

$$S_{ij} = \frac{A_{ij}}{A_{(LNPP, j)}} \tag{7}$$

where S_{ij} is the sensitivity index of factor i in year j and $A_{(LNPP, j)}$ is the anomaly of LNPP in year j.

Due to the indirect effect of ocean warming on LNPP variability, the sensitivity of land drivers to ocean warming was further analyzed by the Granger causality test. The Granger causality test is a popular method for testing causal inference in temporal data and detecting interaction relationships between vegetation variation and climate
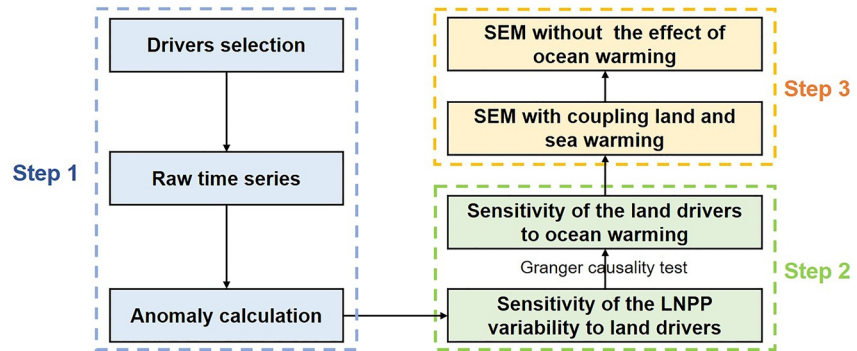
Figure 3. Step-by-step procedure for detecting the effects of coupled land-sea warming on the land net primary productivity (LNPP) variability based on the structural equation model (SEM) analysis.

change (Jiang et al., 2015; Kong et al., 2018). The Granger causality test was performed in R software using the bruceR and lmtest packages.

2.5.2. Construction of the SEM Coupling Land-Sea Warming

After data manipulations were complete, an SEM coupling land and sea warming was established based on known or hypothetical effects and relationships among climate factors, LNPP, and LAI anomalies. The SEM analysis with databases was performed in R software using the lavaan and semPlot packages to test whether and how the coupled land-sea warming affected the LNPP variability. A good model fit was indicated by $0.05 \leq P$ (chi-square) ≤ 1.00, CFI ≥ 0.9, and $0 \leq$ SRMR ≤ 0.05 (SRMR is the standardized root mean square residual). To test whether it had better performance when coupling land and sea warming, the other SEM without the effect of ocean warming was built to compare with that of coupling land and sea warming. The detailed step-by-step procedure for the SEM analysis can be seen in Figure 3.

2.6. Contribution of Climate Warming and Urbanization to LNPP Variability

By isolating the impacts of urbanization and climate on the variability of LNPP, we identified the urbanization-induced LNPP variation by overlaying the map of the urbanization-dominant areas with the LNPP trend. Climate-driven LNPP variation was identified by overlaying the map of climate-dominant areas with the LNPP trend. Afterward, the relative contributions of urban expansion (C_{ue}), climate warming (C_{cw}), and land cover change (C_{lcc}) were determined as proportions between the trends of climate-driven LNPP change, urbanization-induced LNPP change, LCC-induced LNPP change and the sum of their absolute values. The equations of percent contribution are as follows:

$$C_{ue} = \frac{|\Delta Urb|}{|\Delta Clim| + |\Delta Urb| + |\Delta LCC|} \times 100\% \tag{8}$$

$$C_{cw} = \frac{|\Delta Clim|}{|\Delta Clim| + |\Delta Urb| + |\Delta LCC|} \times 100\% \tag{9}$$

$$C_{lcc} = \frac{|\Delta LCC|}{|\Delta Clim| + |\Delta Urb| + |\Delta LCC|} \times 100\% \tag{10}$$

where $|\Delta Urb|$ is the absolute value of urbanization-induced LNPP change; $|\Delta Clim|$ is the absolute value of climate-driven LNPP change; $|\Delta LCC|$ is the absolute value of LCC-induced LNPP change.

The value of climate-driven LNPP change ($\Delta Clim$), urbanization-induced LNPP change (ΔUrb), and LCC-induced LNPP change (ΔLCC) were calculated by the following equations:

$$\Delta Clim = \sum_{i=1}^{n} \beta_i \times \Delta t \tag{11}$$

$$\Delta Urb = \sum_{j=1}^{n} \beta_j \times \Delta t \tag{12}$$

$$\Delta LCC = \sum_{k=1}^{n} \beta_k \times \Delta t \tag{13}$$

where β_i, β_j, and β_k are the slope of the LNPP trend in *the i*th pixel of climate-dominant areas, *j*th pixel of urbanization-dominant areas, and *k*th pixel of LCC-dominant areas, respectively. Δt is the temporal span from 1985 to 2015. The unit of $\Delta Clim$, ΔUrb, ΔLCC is TgC.

We further calculated the contribution of each climate factor to the variability in LNPP based on the SEM analysis. If there was a directly connected path between two factors (e.g., precipitation and LNPP), the contribution of precipitation to LNPP was the standardized path coefficient; if there was an indirectly connected path between two factors (e.g., SST and LNPP), the contribution of SST to LNPP was produced by multiplying all the standardized path coefficients on the connected paths. In addition, the contribution of climatic factors to LNPP was the sum of standardized direct and indirect path coefficients. The functions are as follows:

$$\text{Direct effects } C_{ij} = \gamma_{ij} \tag{14}$$

$$\text{Indirect effects } C_{ij} = \prod_{m=n-1}^{n} \gamma_{ij} \tag{15}$$

$$\text{Total effect } C_{ij} = C_{(D)ij} + C_{(I)ij} \tag{16}$$

where C_{ij} is the contribution of variable i to j, γ_{ij} is the standardized path coefficient between i and j, n is the number of connected paths between i and j, and m is the number of connected variables between i and j.

3. Results

### 3.1. The Spatiotemporal Variation of LNPP Near the NSCS

The annual LNPP near the NSCS presented a significant turning point in 2003 in the piecewise linear regression and showed a slow increase during 1985–2003 but a sharp decline after 2003 and then a slow increase again during 2004–2015 (Figure 4a). There was large spatial heterogeneity in the annual LNPP variation before 2003. For most regions, the annual LNPP turning time occurred in 2003, and turning point types were mainly focused on positive reversal and interrupted increase (Figure 4b). Positive reversal suggested a shift in annual LNPP from a decreasing trend to an increase around 2003, and an interrupted increase presented a shift in annual LNPP from an increasing trend toward a faster or slower increase around 2003.

In the whole region, the total LNPP loss was 0.40 Tg C from 1985 to 2015. In different land use/cover types, all land use/cover types showed a decreasing trend of annual LNPP with the largest decline in cropland and forest (Figure 4c and Table S1 in Supporting Information S1). The spatial pattern of the annual LNPP trend with significant spatial heterogeneity presented an overall decrease (the count of significant decrease was almost three times more than significant increase), which showed a significant decrease in most inner regions but a significant increase in the northeast and southwest regions (Figure 4d).

3.2. Effects of Coupled Land-Sea Warming on the LNPP Variability

To identify the key drivers and mechanism of the LNPP turning point in 2003, we built structural equation models of the effects of coupled land-sea warming on annual LNPP variability focusing on climate dominance areas. First, the sensitivity analysis of the LNPP variation to drivers was analyzed to prepare for the SEM construction. We observed a sharp decline (turning point) in the LNPP after 2003 and used the negative values (subset values) of the LNPP anomaly to analyze the sensitivity of the declined LNPP to drivers and test how the coupled land-sea warming affected the sharp decline in the LNPP after 2003. Figure 5 showed the results of the sensitivity analysis of the LNPP anomaly to driver anomalies. The precipitation and SMC anomalies positively promoted the annual LNPP turning after 2003, which indicated the possible relationship between LNPP turning and abnormally low
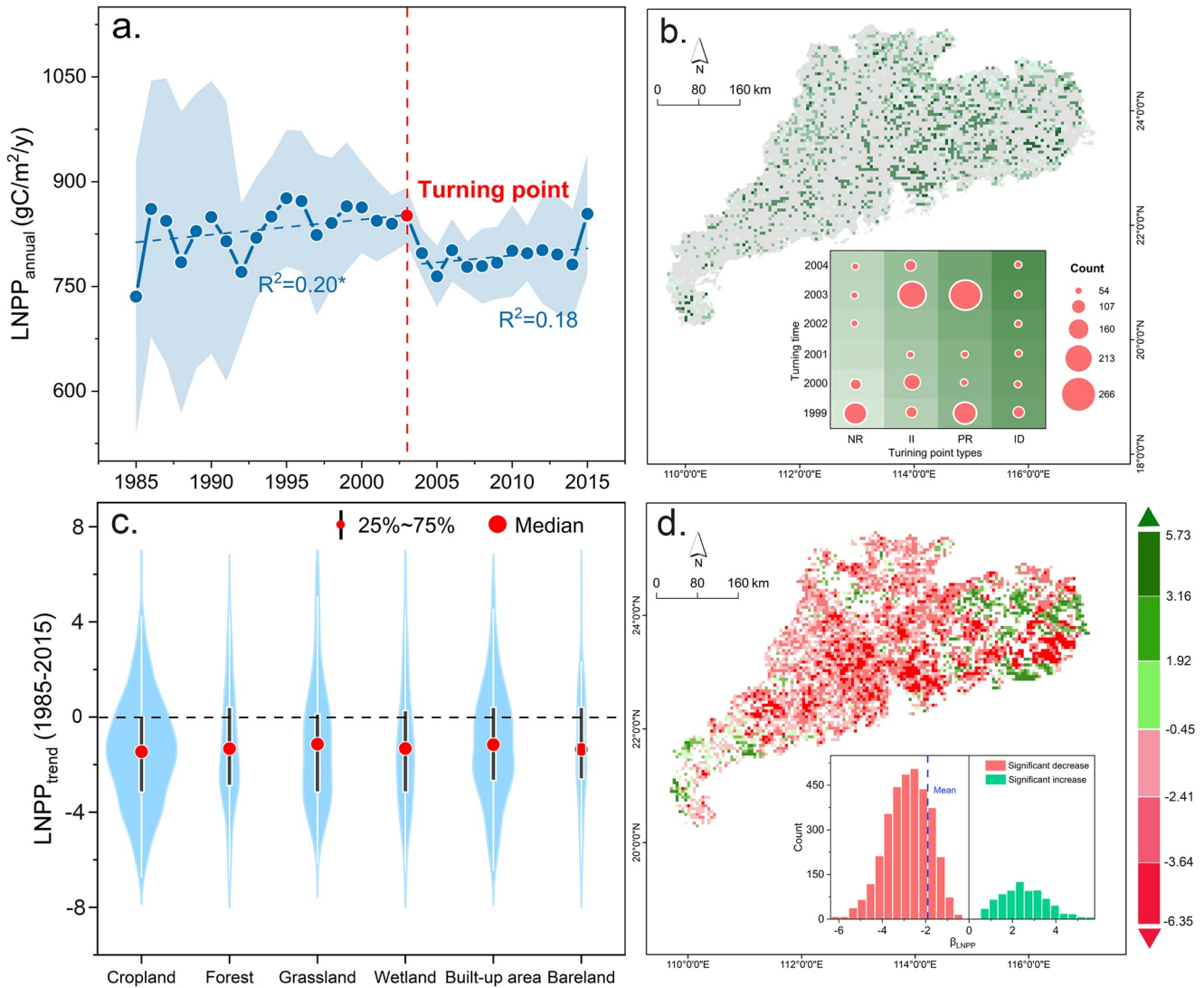
Figure 4. The spatiotemporal dynamics of annual land net primary productivity (LNPP) from 1985 to 2015. (a) Temporal dynamics of annual LNPP (light blue shade is spatial error range); (b) spatial distribution of turning time and turning point types of annual LNPP (NR: negative reversal, II: interrupted increase, PR: positive reversal, ID: interrupted decrease); (c) the trend of annual LNPP in different land use/cover types (light blue shade is distribution range of data); (d) spatial dynamics of annual LNPP.

rainfall and moisture (Figures 5a and 5d). However, the LST, ASH, and VPD anomalies reversely promoted LNPP turning after 2003 (Figures 5b and 5c), suggesting the possible relationship between LNPP turning and abnormally high LST and VPD.

Afterward, the Granger causality test was applied to detect the coupled relationship between land and sea warming (e.g., SST anomaly and LST anomaly, oceanic evaporation anomaly, and land humidity anomaly). Our results suggested a high consistency in interannual variability between the SST anomaly and LST anomaly in the GBA (Figure 6a). The LST anomaly and SST anomaly were mutually affected, and the LST anomaly was amplified by the SST anomaly, which was consistent with global observations of land/sea surface temperature (Byrne & O'Gorman, 2018). The oceanic evaporation anomaly was affected by the land relative humidity anomaly, and there was a 2-year lag time on the impact of the oceanic evaporation anomaly on the land relative humidity anomaly (Figure 6b).

Finally, two SEMs of coupled land-sea warming and not considering ocean warming were constructed, and the results showed that the model had better performance and could better explain the interannual variability in the
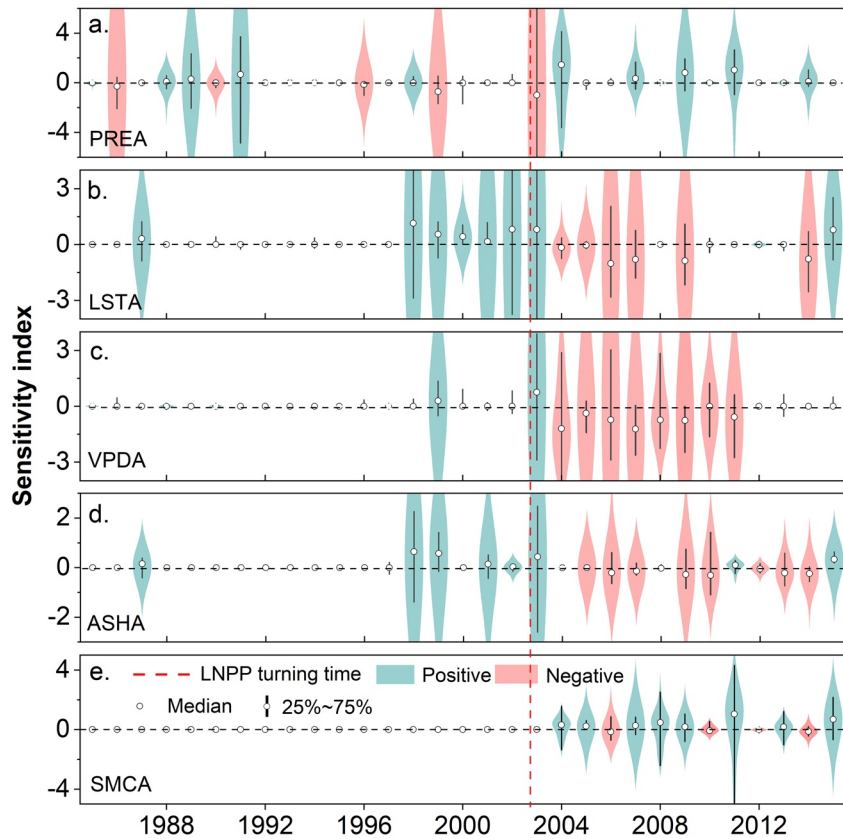
**Figure 5.** (a–e) Sensitivity analysis of the annual land net primary productivity (LNPP) anomaly to the precipitation anomaly (PREA), land surface temperature anomaly (LSTA), vapor pressure deficit anomaly (VPDA), atmospheric specific humidity anomaly (ASHA), and soil moisture content anomaly (SMCA). The negative and positive sensitivity indices present a negative and positive correlation between the LNPP anomaly and driver anomaly, respectively.

LNPP when coupled land-sea warming was considered (Figure 7). Figure 7b shows the results of the SEM analysis with coupled land-sea warming. The LAI anomaly and LNPP anomaly were significantly negatively related to the VPD anomaly ($\gamma = -0.34$ and -0.76, $p < 0.001$), where γ was the standardized path coefficient. SEM analysis was further used to evaluate the indirect effects of the SST and LST anomalies on the LNPP anomaly, and we
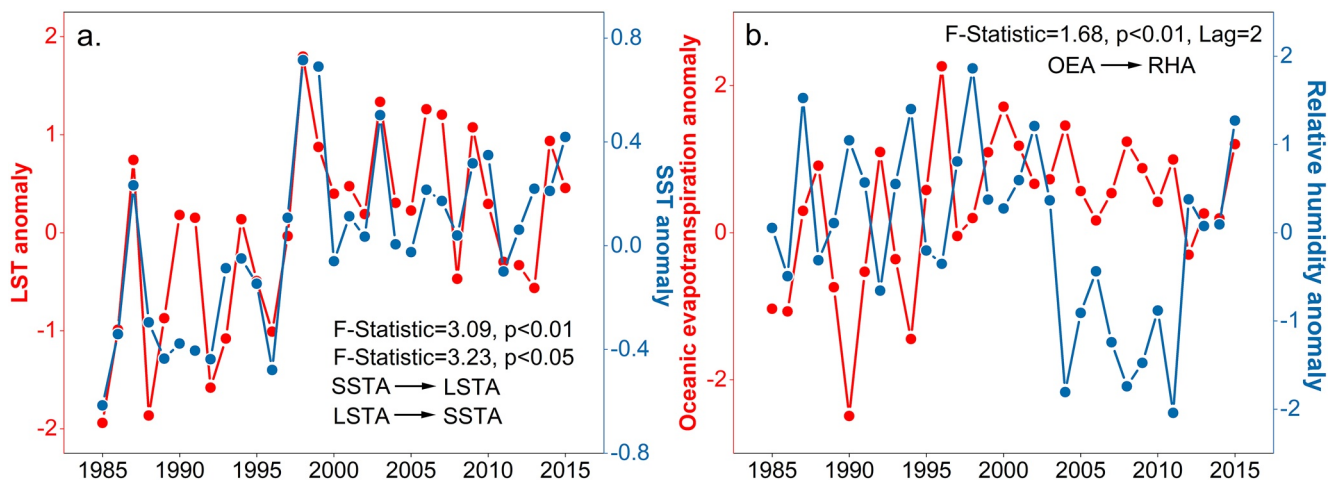
Figure 6. The Granger causality test of Northern South China Sea (NSCS) ocean warming and land climate change. (a) The interaction of the sea surface temperature (SST) anomaly (SSTA) and land surface temperature (LST) anomaly (LSTA); (b) the interaction of the oceanic evaporation anomaly (OEA) and relative humidity anomaly (RHA).
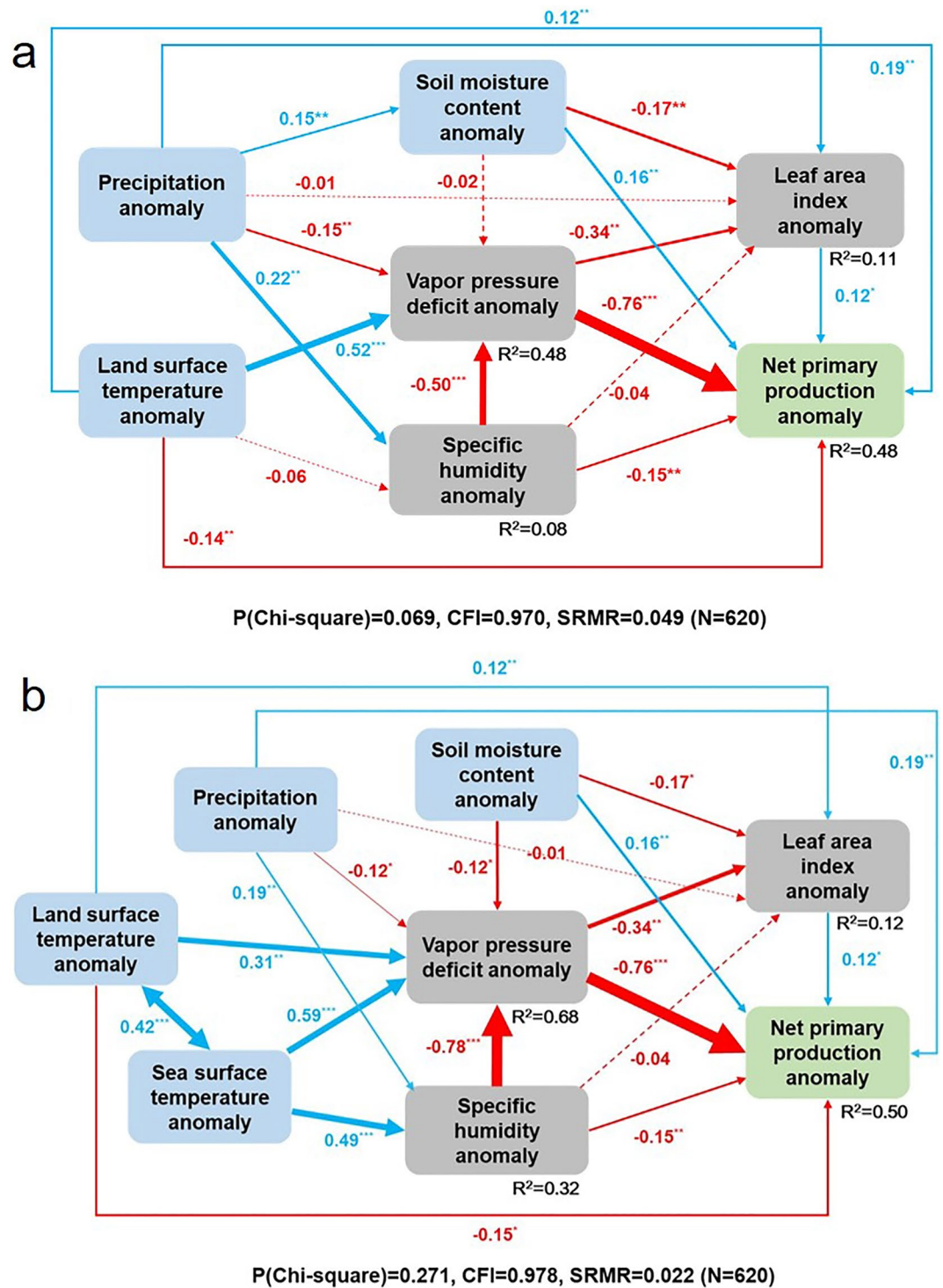
Figure 7. Structural equation models of coupled land-sea warming effects on the inter-annual variability and turning of land net primary productivity (LNPP) in the Greater Bay Area (GBA), including the structural equation model (SEM) without ocean warming (a) and with the coupled land-sea warming (b). The solid arrows represent significant effects (*$p < 0.05$, **$p < 0.01$, ***$p < 0.001$), dashed arrows represent nonsignificant effects ($p > 0.05$), the width of arrows represents the intensity of standardized path coefficients, and the numbers on the arrows are standardized path coefficients. The blue boxes represent explanatory variables, the green box represents the dependent variables and the dark gray boxes represent mediator variables in the model.

Table 1
Contributions of Climatic Drivers and Urbanization to LNPP Variability

Drivers	NPP change (TgC)	Area (km²)	Proportion (%)	Sub-Drivers	Direct effects (γ)	Proportion (%)	Indirect effects (γ)	Proportion (%)
Climate	−0.20	3688.02	50.00	SMCA	0.16	11.34	0.07	5.43
				LSTA	−0.15	10.64	−0.25	19.38
				SSTA			−0.26	20.16
				PREA	0.19	13.47	0.06	4.65
				ASHA	−0.15	10.64		
				VPDA	−0.76	53.91		
Urbanization	−0.16	190.21	40.00					
Land cover change	−0.04	79.23	10.00					

observed that the SST and LST anomalies presented a significant indirect effect on the LNPP anomaly ($\gamma = -0.26$ and -0.25, respectively). We also observed that the SST anomaly presented a significant direct effect and was positively related to the VPD anomaly ($\gamma = 0.59$, $p < 0.001$), but the atmospheric specific humidity (ASH) anomaly presented a stronger direct effect and was negatively related to the VPD anomaly ($\gamma = -0.78$, $p < 0.001$). The LST anomaly presented a significant direct effect and was positively related to the VPD anomaly ($\gamma = 0.31$, $p < 0.01$). The model identified the VPD anomaly as a major direct driver of the annual LNPP anomaly and turning point, and the SST and LST anomalies were the major indirect drivers. To explain our SEM results, other possible SEMs were supplemented in the Supplementary materials (Figure S3 in Supporting Information S1), and the correlations between all the analyzed variables in the SEMs were also supplemented in the Supporting Information S1 (Figure S4).

3.3. Contribution of Climate Warming and Urbanization to LNPP Variability

By isolating the impacts of climate warming, urbanization, and LCC on LNPP variability, we identified climate-driven, urbanization-driven, and LCC-driven LNPP changes and calculated the proportions of the contribution of the three drivers to the LNPP anomaly. The results suggested that climate warming and urbanization were the determinant factors of LNPP variability near the NSCS, accounting for 50.00% and 40.00%, respectively (Table 1). In addition to the serious decline in LNPP (0.20 Tg C) caused by climate warming, urbanization also caused a large loss in LNPP (0.16 Tg C). To clarify the contribution of each climate factor to the variability in LNPP under coupled land-sea warming, we further calculated the percent contribution index of each climate factor and identified the key factors among climate drivers. The results showed that the VPDA was the key direct contributor to LNPP variability with contributions of 53.91% (Figure 8a and Table 1), and the SSTA and LSTA were the two indirect contributors with contributions of 20.16%, and 19.38%, respectively (Figure 8b and Table 1).

4. Discussion

4.1. VPD Change Explained Spatiotemporal Variation of LNPP

Changes in water availability determined by temperature and humidity variation are becoming the dominant drivers of global vegetation productivity change (Murray-Tortarolo et al., 2016; O'Sullivan et al., 2020). Our results showed that annual LNPP had a similar trend with the relative humidity but an opposite trend with the VPD after 2003 (Figure S5 in Supporting Information S1). A reduced relative humidity, indicating water stress conditions and atmospheric dryness, caused an increase in the VPD (Figure S5 in Supporting Information S1), which triggered stomatal closure to conserve water and caused vegetation evapotranspiration and photosynthesis decline (Pascolini-Campbell et al., 2021; Xiao et al., 2020). Additionally, the SEM results showed that the VPD anomaly and LST anomaly had strong direct and indirect effects on the LNPP anomaly, respectively, in most of the GBA (Figure 7). The VPD and LST increase near the NSCS indicated that the water availability decline was positively related to the LNPP decrease.
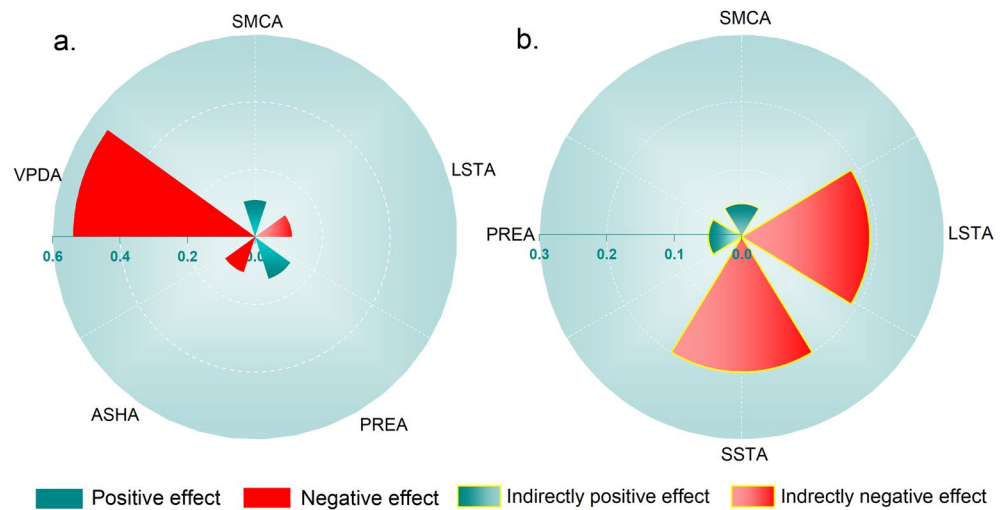
Figure 8. (a) Contributions of direct climate drivers to land net primary productivity (LNPP) variability; (b) contributions of indirect climate drivers to LNPP variability, including the soil moisture content anomaly (SMCA), land surface temperature anomaly (LSTA), sea surface temperature anomaly (SSTA), precipitation anomaly (PREA), atmospheric specific humidity anomaly (ASHA), and vapor pressure deficit anomaly (VPDA).

Most of the global variability in modeled land carbon uptake is driven by temperature and vapor pressure deficit effects that are controlled by soil moisture (Humphrey et al., 2021). Soil moisture-atmosphere feedbacks play a key role in land carbon uptake variability under drought stress (O'Sullivan et al., 2020). In our study, we observed that soil moisture had a significant correlation but a low effect (standardized path coefficient $\gamma = 0.16$) of soil moisture on LNPP variability (Figure 7). Some studies have suggested that the stomata of the leaves effectively expand and photosynthesis is promoted when the soil moisture supply is sufficient to support leaf evaporation (Bateni & Entekhabi, 2012; Yin et al., 2014). However, they have not considered the effect of the VPD driven by reduced vapor transport from the ocean on plant photosynthesis. In this case, even if the soil moisture supply is sufficient, the plant leaf stomata will close to prevent water loss as the vapor pressure deficit increases. However, soil moisture-atmosphere feedback (soil moisture-vapor pressure deficit) is likely to be an important factor for land carbon uptake in the future near the NSCS because the increasing trend of the global VPD will continue to the end of the 21st century according to the predictions of global climate models (Yuan et al., 2019), and the soil moisture gradually decreased after 2013 in the GBA (Figure S6 in Supporting Information S1).

4.2. Coupled Land-Sea Warming Driven VPD Increase

Global warming has become severe in recent decades due to anthropogenic CO_2 and heat emissions (Abatzoglou et al., 2019). Additionally, the ocean became warmer because 30% of anthropogenic CO_2 and heat have sunk into the ocean every year (Bronselaer & Zanna, 2020; Resplandy et al., 2018). Ocean warming in turn increases land surface temperature and specific humidity to balance the moist static energy over the land and ocean (Byrne & O'Gorman, 2018). A recent study suggested that there was a strong coupling relationship between summer temperature and humidity anomalies and SST anomalies in coastal cities during a marine heatwave (Hu, 2021).

Approximately 85% of atmospheric water vapor is evaporated from the surrounding oceans, with the remaining 15% coming from evaporation and transpiration over terrestrial ecosystems (Trenberth et al., 2007). Although atmospheric specific humidity increased as oceanic evaporation increased under sea surface temperature increases in recent decades (IPCC, 2021), coupled land-sea warming caused an increase in atmospheric specific humidity and a decrease in relative humidity over land. Finally, the land VPD increased under this trend.

As the land VPD increased, leaf stomata contracted to prevent water loss when leaf water evaporation was greater than the soil moisture supply under drought stress, which is not conducive to plant photosynthesis (Ding et al., 2018; Novick et al., 2016). Therefore, we proposed a hypothesis that land and neighboring ocean warming in the GBA increases near the land VPD and further decreases LNPP. SEM analysis was adopted to prove our hypothesis, and the model results showed that LNPPA was indirectly negatively correlated with the coupled

land-sea warming ($\gamma = -0.51$) (Figure 7 and Table 1). The VPD increase due to coupled land-sea warming was identified as a major driver of the LNPP decrease in most of the GBA, which was consistent with our hypothesis.

4.3. The Relative Importance of Urbanization Compared With Climate Warming in LNPP Variability

Urbanization is one of the key components of human-associated disturbance, and its effects on LNPP have been widely examined (Imhoff et al., 2004; Jia et al., 2018). In general, impervious surface increases with urbanization directly caused vegetation decreases and declines in NPP, but urbanization indirectly enhanced vegetation growth by increasing urban temperature and CO_2 concentration, which can offset 30% of the direct negative impact of urbanization (Zhao et al., 2016). However, the overall negative effect of urbanization on NPP is much greater than the positive effect. Our results suggested that land regions near the NSCS experienced rapid urbanization from 1985 to 2015, especially in the GBA. A large amount of cropland and forest were converted into built-up areas, which caused a large loss in LNPP due to urbanization (Figure S7 in Supporting Information S1). This finding was consistent with previous research (Zhang et al., 2021). Globally, rapid urbanization in the past decade has caused a net loss of 22.4 TgC in terrestrial NPP, and although this is small compared to the total terrestrial carbon sink and anthropogenic CO_2 emissions worldwide, the urbanization-driven decrease in NPP offset 30% of the climate-driven increase from 2000 to 2010 (Liu et al., 2019). In our study, the LNPP in built-up areas presented a decreasing trend from 1985 to 2015 driven by rapid urbanization (Figure 4c), which was consistent with previous research (Cao et al., 2004; Zhang et al., 2021). Rapid urbanization in the past several decades has caused a net loss of 0.16 TgC in LNPP and an increase of 190 km^2 in newly built-up areas near the NSCS. Compared with the climate-driven decrease in LNPP, the reduced LNPP per unit area driven by urbanization was much greater than that driven by climate warming, approximately 19 times higher than the climate-driven reduced LNPP per unit area (Table 1). Thus, vegetal losses driven by urbanization were equally important for LNPP variability compared with climate warming from a long-term perspective. The interaction of urbanization and climate warming needs to be considered when formulating strategies for reducing CO_2 emissions, increasing sinks, and mitigating climate change.

5. Conclusions

Our study focuses on the impact of land-sea warming interactions on coastal ecosystem services under global warming, and the mechanism by which land-sea warming affects the carbon uptake of terrestrial ecosystems was explored based on the theory of land-sea water vapor transport and ocean amplification of land temperature. Climate warming, LCC, and urbanization were integrated to reveal the dominant factors of LNPP variability under climate change and human activities. We found that vapor transported from the ocean to land decreased and relative humidity decreased over land owing to land and neighboring ocean warming in the GBA, therefore resulting in an increase in VPD over land, and this effect reduced vegetation photosynthesis and land net carbon uptake on the south coast of China. Atmospheric VPD, as a characterization of land surface humidity anomaly, was the key direct driver affecting land net carbon uptake, accounting for 53.91%. Additionally, coupled land-sea warming had a significant indirect effect on terrestrial carbon uptake with a contribution of 39.54%. Urbanization led to a large loss in LNPP, which was slightly less than the decrease in LNPP driven by climate warming.

Our results revealed coupled land-sea warming as a dominant factor in the spatial-temporal evolution and variability of regional carbon uptake in the Guangdong, Hong Kong, and Macau regions, which can improve the carbon flux model of regional ecosystems and inform the formulation of regional climate change mitigation strategies and the realization of regional carbon peak and carbon neutrality goals.

Abbreviations

ASH	atmospheric specific humidity
ASHA	atmospheric specific humidity anomaly
GBA	Guangdong-HongKong-Macao Greater Bay Area
LAI	leaf area index
LAIA	leaf area index anomaly
LCC	land cover change

LNPP	land net primary production
LNPPA	land net primary production anomaly
LST	land surface temperature
LSTA	land surface temperature anomaly
NCU	net carbon uptake
NSCS	Northern South China Sea
OEA	oceanic evaporation anomaly
PREA	precipitation anomaly
RHA	relative humidity anomaly
SEM	structural equation model
SST	sea surface temperature
SSTA	sea surface temperature anomaly
SMC	soil moisture content
SMCA	soil moisture content anomaly
VPD	vapor pressure deficit
VPDA	vapor pressure deficit anomaly

Conflict of Interest

The authors declare no conflicts of interest relevant to this study.

Data Availability Statement

All data sources used in our study are provided in the Data sources section. All data needed to evaluate the conclusions are available at Supporting Information S1 and figshare (https://doi.org/10.6084/m9.figshare.17087336).

References

Abatzoglou, J. T., Williams, A. P., & Barbero, R. (2019). Global emergence of anthropogenic climate change in fire weather indices. *Geophysical Research Letters*, *46*, 326–336. https://doi.org/10.1029/2018GL080959

Arias-Ortiz, A., Serrano, O., Masqué, P., Lavery, P. S., Mueller, U., Kendrick, G. A., et al. (2018). A marine heatwave drives massive losses from the world's largest seagrass carbon stocks. *Nature Climate Change*, *8*(4), 338–344. https://doi.org/10.1038/s41558-018-0096-y

Ballantyne, A. P., Alden, C. B., Miller, J. B., Tans, P. P., & White, J. W. C. (2012). Increase in observed net carbon dioxide uptake by land and oceans during the past 50 years. *Nature*, *488*(7409), 70–72. https://doi.org/10.1038/nature11299

Bastos, A., & Fleischer, K. (2021). Effects of rising CO_2 levels on carbon sequestrat. *Nature*, *591*, 532–534. https://doi.org/10.1038/d41586-021-00737-1

Bastos, A., Running, S. W., Gouveia, C., & Trigo, R. M. (2013). The global NPP dependence on ENSO: La Niña and the extraordinary year of 2011. *Journal of Geophysical Research: Biogeosciences*, *118*, 1247–1255. https://doi.org/10.1002/jgrg.20100

Bateni, S. M., & Entekhabi, D. (2012). Relative efficiency of land surface energy balance components. *Water Resources Research*, *48*, W04510. https://doi.org/10.1029/2011WR011357

Bernardino, P. N., De Keersmaecker, W., Fensholt, R., Verbesselt, J., Somers, B., & Horion, S. (2020). Global-scale characterization of turning points in arid and semi-arid ecosystem functioning. *Global Ecology and Biogeography*, *29*(7), 1230–1245. https://doi.org/10.1111/geb.13099

Bronselaer, B., & Zanna, L. (2020). Heat and carbon coupling reveals ocean warming due to circulation changes. *Nature*, *584*(7820), 227–233. https://doi.org/10.1038/s41586-020-2573-5

Byrne, M. P., & O'Gorman, P. A. (2013). Link between land-ocean warming contrast and surface relative humidities in simulations with coupled climate models. *Geophysical Research Letters*, *40*, 5223–5227. https://doi.org/10.1002/grl.50971

Byrne, M. P., & O'Gorman, P. A. (2018). Trends in continental temperature and humidity directly linked to ocean warming. *Proceedings of the National Academy of Sciences of the United States of America*, *115*, 4863–4868. https://doi.org/10.1073/pnas.1722312115

Cao, M., Prince, S. D., Small, J., & Goetz, S. J. (2004). Remotely sensed interannual variations and trends in terrestrial net primary productivity 1981–2000. *Ecosystems*, *7*(3), 233–242. https://doi.org/10.1007/s10021-003-0189-x

Carnicer, J., Domingo-Marimon, C., Ninyerola, M., Camarero, J. J., Bastos, A., López-Parages, J., et al. (2019). Regime shifts of Mediterranean forest carbon uptake and reduced resilience driven by multidecadal ocean surface temperatures. *Global Change Biology*, *25*(8), 2825–2840. https://doi.org/10.1111/gcb.14664

Chen, J., Cao, X., Peng, S., & Ren, H. (2017). Analysis and applications of GlobeLand30: A review. *ISPRS International Journal of Geo-Information*, 6(8), 230. https://doi.org/10.3390/ijgi6080230

Ding, J., Yang, T., Zhao, Y., Liu, D., Wang, X., Yao, Y., et al. (2018). Increasingly important role of atmospheric aridity on Tibetan alpine grasslands. *Geophysical Research Letters*, *45*, 2852–2859. https://doi.org/10.1002/2017GL076803

Ding, Z. H., Peng, J., Qiu, S. J., & Zhao, Y. (2020). Nearly half of global vegetated area experienced Inconsistent vegetation growth in terms of Greenness, cover, and productivity. *Earth's Future*, *12*, e2020EF001618. https://doi.org/10.1029/2020EF001618

Frölicher, T. L., Fischer, E. M., & Gruber, N. (2018). Marine heatwaves under global warming. *Nature*, *560*(7718), 360–364. https://doi.org/10.1038/s41586-018-0383-9

Grossiord, C., Buckley, T. N., Cernusak, L. A., Novick, K. A., Poulter, B., Siegwolf, R. T. W., et al. (2020). Plant responses to rising vapor pressure deficit. *New Phytologist*, *226*(6), 1550–1566. https://doi.org/10.1111/nph.16485

Harris, I., Jones, P. D., Osborn, T. J., & Lister, D. H. (2014). Updated high-resolution grids of monthly climatic observations—The CRU TS3.10 Dataset. *International Journal of Climatology*, *34*(3), 623–642. https://doi.org/10.1002/joc.3711

Hu, L. Q. (2021). A global assessment of coastal marine heatwaves and their relation with coastal urban thermal changes. *Geophysical Research Letters*, *48*, e2021GL093260. https://doi.org/10.1029/2021GL093260

Hu, Z., Yu, G., Fu, Y., Sun, X., Li, Y., Shi, P., & Zheng, Z. (2008). Effects of vegetation control on ecosystem water use efficiency within and among four grassland ecosystems in China. *Global Change Biology*, *14*(7), 1609–1619. https://doi.org/10.1111/j.1365-2486.2008.01582.x

Humphrey, V., Berg, A., Ciais, P., Gentine, P., Jung, M., Reichstein, M., et al. (2021). Soil moisture-atmosphere feedback dominates land carbon uptake variability. *Nature*, *592*(7852), 65–69. https://doi.org/10.1038/s41586-021-03325-5

Imhoff, M. L., Bounoua, L., DeFries, R., Lawrence, W. T., Stutzer, D., Tucker, C. J., & Ricketts, T. (2004). The consequences of urban land transformation on net primary productivity in the United States. *Remote Sensing of Environment*, *89*(4), 434–443. https://doi.org/10.1016/j.rse.2003.10.015

IPCC. (2021). Climate change 2021: The physical science basis. In V.Masson-Delmotte, P.Zhai, A.Pirani, S. L.Connors, C.Péan, S.Berger, et al. (Eds.), *Contribution of Working Group I to the Sixth Assessment Report of the Intergovernmental Panel on climate change*. Cambridge University Press.

Jia, W., Zhao, S., & Liu, S. (2018). Vegetation growth enhancement in urban environments of the Conterminous United States. *Global Change Biology*, *24*(9), 4084–4094. https://doi.org/10.1111/gcb.14317

Jiang, B., Liang, S., & Yuan, W. (2015). Observational evidence for impacts of vegetation change on local surface climate over northern China using the Granger causality test. *Journal of Geophysical Research: Biogeosciences*, *120*, 1–12. https://doi.org/10.1002/2014JG002741

Kong, D., Miao, C., Duan, Q., Lei, X., & Li, H. (2018). Vegetation-climate interactions on the loess plateau: A nonlinear Granger causality analysis. *Journal of Geophysical Research: Atmospheres*, *123*, 11608–11079. https://doi.org/10.1029/2018JD029036

Liu, X., Pei, F., Wen, Y., Li, X., Wang, S., Wu, C., et al. (2019). Global urban expansion offsets climate-driven increases in terrestrial net primary productivity. *Nature Communications*, *10*(1), 5558. https://doi.org/10.1038/s41467-019-13462-1

Liu, Y., Parolari, A. J., Kumar, M., Huang, C.-W., Katul, G. G., & Porporato, A. (2017). Increasing atmospheric humidity and CO_2 concentration alleviate forest mortality risk. *Proceedings of the National Academy of Sciences of the United States of America*, *114*(37), 9918–9923. https://doi.org/10.1073/pnas.1704811114

Lucht, W., Prentice, I. C., Myneni, R. B., Sitch, S., Friedlingstein, P., Cramer, W., et al. (2002). Climatic control of the high-latitude vegetation greening trend and Pinatubo effect. *Science*, *296*(5573), 1687–1689. https://doi.org/10.1126/science.1071828

Luo, T. X. (1996). *Patterns of net primary productivity for Chinese major forest types and their mathematical models* (PhD dissertation). Chinese Academy of Sciences.

Massmann, A., Gentine, P., & Lin, C. J. (2019). When does vapor pressure deficit drive or reduce evapotranspiration. *Journal of Advances in Modeling Earth Systems*, *11*, 3305–3320. https://doi.org/10.1029/2019MS001790

Murray-Tortarolo, G., Friedlingstein, P., Sitch, S., Seneviratne, S. I., Fletcher, I., Mueller, B., et al. (2016). The dry season intensity as a key driver of NPP trends. *Geophysical Research Letters*, *43*, 2632–2639. https://doi.org/10.1002/2016GL068240

Novick, K. A., Ficklin, D. L., Stoy, P. C., Williams, C. A., Bohrer, G., Oishi, A. C., et al. (2016). The increasing importance of atmospheric demand for ecosystem water and carbon fluxes. *Nature Climate Change*, *6*(11), 1023–1027. https://doi.org/10.1038/nclimate3114

O'Sullivan, M., Smith, W. K., Sitch, S., Friedlingstein, P., Arora, V. K., Haverd, V., et al. (2020). Climate-driven variability and trends in plant productivity over recent decades based on three global products. *Global Biogeochemical Cycles*, *34*, e2020GB006613. https://doi.org/10.1029/2020GB006613

Pascolini-Campbell, M., Reager, J. T., Chandanpurkar, H. A., & Rodell, M. (2021). A 10 per cent increase in global land evapotranspiration from 2003 to 2019. *Nature*, *593*(7860), 543–547. https://doi.org/10.1038/s41586-021-03503-5

Pei, F., Li, X., Liu, X., Wang, S., & He, Z. (2013). Assessing the differences in net primary productivity between pre- and post-urban land development in China. *Agricultural and Forest Meteorology*, *171–172*(3), 174–186. https://doi.org/10.1016/j.agrformet.2012.12.003

Piao, S., Ciais, P., Friedlingstein, P., Peylin, P., Reichstein, M., Luyssaert, S., et al. (2008). Net carbon dioxide losses of northern ecosystems in response to autumn warming. *Nature*, *451*(7174), 49–52. https://doi.org/10.1038/nature06444

Rajah, K., O'Leary, T., Turner, A., Petrakis, G., Leonard, M., & Westra, S. (2014). Changes to the temporal distribution of daily precipitation. *Geophysical Research Letters*, *41*, 8887–8894. https://doi.org/10.1002/2014GL062156

Resplandy, L., Keeling, R. F., Eddebbar, Y., Brooks, M. K., Wang, R., Bopp, L., et al. (2018). Quantification of ocean heat uptake from changes in atmospheric O_2 and CO_2 composition. *Nature*, *563*(7729), 105–108. https://doi.org/10.1038/s41586-018-0651-8

Runyon, J., & Waring, R. H. (1994). Environmental limits on net primary production and light-use efficiency across the Oregon Transect. *Ecological Application*, *4*(2), 226–237. https://doi.org/10.2307/1941929

Smale, D. A., Wernberg, T., Oliver, E. C. J., Thomsen, M., Harvey, B. P., Straub, S. C., et al. (2019). Marine heatwaves threaten global biodiversity and the provision of ecosystem services. *Nature Climate Chang*, *9*(4), 306–312. https://doi.org/10.1038/s41558-019-0412-1

Sutton, R. T., Dong, B., & Gregory, J. M. (2007). land/sea warming ratio in response to climate change: IPCC AR4 model results and comparison with observations. *Geophysical Research Letters*, *34*, L02701. https://doi.org/10.1029/2006GL028164

Tkachenko, K. S., & Soong, K. (2017). Dongsha Atoll: A potential thermal refuge for reef-building corals in the south China sea. *Marine Environmental Research*, *127*, 112–125. https://doi.org/10.1016/j.marenvres.2017.04.003

Trenberth, K. E., Smith, L., Qian, T., Dai, A., & Fasullo, J. (2007). Estimates of the global water budget and its annual cycle using observational and model data. *Journal of Hydrometeorology*, *8*, 758–769. https://doi.org/10.1175/JHM600.1

Ukkola, A. M., Prentice, I. C., Keenan, T. F., van Dijk, A. I. J. M., Viney, N. R., Myneni, R. B., & Bi, J. (2016). Reduced streamflow in water-stressed climates consistent with CO_2 effects on vegetation. *Nature Climate Change*, *6*, 75–78. https://doi.org/10.1038/nclimate2831

Wang, X., Piao, S., Ciais, P., Friedlingstein, P., Myneni, R. B., Cox, P., et al. (2014). A two-fold increase of carbon cycle sensitivity to tropical temperature variations. *Nature*, *506*(7487), 212–215. https://doi.org/10.1038/nature12915

Wu, G. L., Cheng, Z., Alatalo, J. M., Zhao, J., & Liu, Y. (2021). Climate warming consistently reduces grassland ecosystem productivity. *Earth's Future*, *9*, e2020EF001837. https://doi.org/10.1029/2020EF001837

Xiao, M., Yu, Z., Kong, D., Gu, X., Mammarella, I., Montagnani, L., et al. (2020). Stomatal response to decreased relative humidity constrains the acceleration of terrestrial evapotranspiration. *Environmental Research Letters*, *15*(9), 094066. https://doi.org/10.1088/1748-9326/ab9967

Yang, Y., Fang, J., Ma, W., & Wang, W. (2008). Relationship between variability in aboveground net primary production and precipitation in global grasslands. *Geophysical Research Letters*, *35*, L23710. https://doi.org/10.1029/2008GL035408

Yin, D. Q., Roderick, M. L., Leech, G., Sun, F. B., & Huang, Y. F. (2014). The contribution of reduction in evaporative cooling to higher surface air temperatures during drought. *Geophysical Research Letters*, *41*, 7891–7897. https://doi.org/10.1002/2014GL062039

Yu, G. R., Wen, X. F., Sun, X. M., Tanner, B. D., Lee, X., & Chen, J. Y. (2006). Overview of ChinaFLUX and evaluation of its eddy covariance measurement. *Agricultural and Forest Meteorology*, *137*(3–4), 125–137. https://doi.org/10.1016/j.agrformet.2006.02.011

Yuan, W. P., Liu, S., Zhou, G. S., Zhou, G. Y., Tieszen, L. L., Baldocchi, D., et al. (2007). Deriving a light use efficiency model from eddy covariance flux data for predicting dailygross primary production across biomes. *Agricultural and Forest Meteorology*, *143*, 189–207. https://doi.org/10.1016/j.agrformet.2006.12.001

Yuan, W. P., Zheng, Y., Piao, S. L., Ciais, P., & Wang, Y. P. (2019). Increased atmospheric vapor pressure deficit reduces global vegetation growth. *Science Advances*, *5*, eaax1396. https://doi.org/10.1126/sciadv.aax1396

Zappa, G., Ceppi, P., & Shepherd, T. G. (2020). Time-evolving sea-surface warming patterns modulate the climate change response of subtropical precipitation over land. *Proceedings of the National Academy of Sciences of the United States of America*, *117*(9), 4539–4545. https://doi.org/10.1073/pnas.1911015117

Zhang, H., Sun, R., Peng, D., Yang, X., Wang, Y., Hu, Y., et al. (2021). Spatiotemporal dynamics of net primary productivity in China's urban lands during 1982–2015. *Remote Sensing*, *13*(3), 400. https://doi.org/10.3390/rs13030400

Zhao, M. S., & Running, S. W. (2010). Drought-induced reduction in global terrestrial net primary production from 2000 to 2009. *Science*, *329*(5994), 936–940. https://doi.org/10.1126/science.1192666

Zhao, S. Q., Liu, S. G., & Zhou, D. C. (2016). Prevalent vegetation growth enhancement in urban environment. *Proceedings of the National Academy of Sciences of the United States of America*, *113*, 6313–6318. https://doi.org/10.1073/pnas.1602312113

Zhu, Z., Piao, S., Myneni, R. B., Huang, M., Zeng, Z., Canadell, J. G., et al. (2016). Greening of the Earth and its drivers. *Nature Climate Change*, *6*(8), 791–795. https://doi.org/10.1038/nclimate3004